



# Low content of $\text{CoO}_x$ supported on nanocrystalline $\text{CeO}_2$ for toluene combustion: The importance of interfaces between active sites and supports

Fangyun Hu<sup>a</sup>, Yue Peng<sup>a,\*</sup>, Jianjun Chen<sup>a,b</sup>, Shuai Liu<sup>a</sup>, Hua Song<sup>a</sup>, Junhua Li<sup>a,b,\*</sup>

<sup>a</sup> School of Environment, Tsinghua University, Beijing 100084, China

<sup>b</sup> State Key Joint Laboratory of Environment Simulation and Pollution Control, Tsinghua University, Beijing 10084, China

## ARTICLE INFO

### Keywords:

Interfaces

Toluene combustion

Nano

Oxygen vacancies

## ABSTRACT

A low content of  $\text{CoO}_x$  (1 wt% Co loading) was deposited on  $\text{CeO}_2$  nanoparticles (CoCe-P), nanorods (CoCe-R) and nanocubes (CoCe-C) for toluene oxidation. The CoCe-P catalyst showed a significantly higher activity than CoCe-R or CoCe-C. Compared with CoCe-C, the temperature of toluene conversion ( $T_{90} = 90^\circ\text{C}$  and  $T_{50} = 50^\circ\text{C}$ ) for CoCe-P decreased by  $\Delta T_{90} = 86^\circ\text{C}$  and  $\Delta T_{50} = 60^\circ\text{C}$ . The reaction rate ( $r$ ,  $\text{mol m}^{-2} \text{s}^{-1}$ ) of the CoCe-P catalyst at  $220^\circ\text{C}$  increased by nine times. The low content of  $\text{CoO}_x$  formed as either nanoparticles or highly dispersed species on the surfaces of different  $\text{CeO}_2$  nanostructures. The different interactions between  $\text{CoO}_x$  and  $\text{CeO}_2$  are intrinsically relevant to the various redox and catalytic properties. There exists a synergistic effect at the interface between  $\text{CoO}_x$  and  $\text{CeO}_2$ . Highly dispersed  $\text{CoO}_x$  species and the increased oxygen vacancies at the interface led to the excellent performance of CoCe-P for toluene oxidation.

## 1. Introduction

Currently, the establishment of strict regulations for reducing the concentration of volatile organic compounds (VOCs) in the environment is extremely urgent [1]. Benzene, toluene and xylenes (BTX), as specific types of VOCs, are harmful to the environment [2,3]. The catalytic oxidation of BTX, is considered as one of the most promising technologies [4]. The transition-metal oxides are treated as the most promising catalysts for the low temperature catalytic combustion of VOCs, mainly because of their low cost [5,6].

Among the various metal oxides,  $\text{CeO}_2$  is a versatile component of catalysts used in air pollution control, mainly due to its high oxygen storage capacity (OSC) and good redox behavior [7,8]. The various shapes of nanoceria provide an ideal platform for the understanding the crystal plane effect of pure ceria catalyst [9]. Mai et al. first observed that nanorod and nanocube had higher OSC compared to nanopolyhedra ceria, the OSC was associated to the exposure of the more reducible {100} and {110} planes in nanoshaped ceria [10]. Hence, tailored  $\text{CeO}_2$  nanostructures leads a prominent improvement in the catalytic performance. And up till now, it is well known that the benefit of nanoshaped  $\text{CeO}_2$  depends on the given reaction [11–15]. For example,  $\text{CeO}_2$  nanorods with {100} and {110} planes were more active in the selective catalytic reduction of  $\text{NO}_x$  [11], and catalytic combustion of chlorobenzene [12]. While  $\text{CeO}_2$  nanocubes exhibited superior

properties in soot combustion [13], and hydrogen oxidation [14]. The present study exhibit that the superior OSC behavior of nanorods and nanocubes with the highly faceted surfaces can be an important tool for generation of active oxygen species [15]. The findings also highlight that the highly active  $\text{CeO}_2$  catalysts rely on the defective surface sites [16]. Hence, the shape modification of ceria at the nanoscale level can offer a fertile way to govern the catalytic activity.

In recent years, research regarding the interface chemistry between active species and nanosupports has become a charming research field [17–27]. This importance is mainly because interfaces could provide junctions with superior redox and catalytic oxidation. Hence, the investigation of interfaces as a function of highly active redox sites could facilitate the design and preparation of highly active catalytic materials. Currently, the support effects of  $\text{CeO}_2$  for several catalytic oxidation reactions including Au/ $\text{CeO}_2$  for the photocatalytic aerobic oxidation of propylene [18]; Pt/ $\text{CeO}_2$  for CO oxidation [19]; Pd/ $\text{CeO}_2$  for CO and propane oxidation [20]; Pt/ $\text{CeO}_2$  for the oxidation of toluene [21];  $\text{MnO}_x/\text{CeO}_2$  for the selective oxidation of amines [22]; NiO/ $\text{CeO}_2$  catalyst for the partial oxidation of methane [24]; CuO/ $\text{CeO}_2$  for CO oxidation [26] have been investigated. These studies suggest that the active planes of a  $\text{CeO}_2$  support induce correspondingly more active supported catalysts, namely, a {110} facet type of support, such as a  $\text{CeO}_2$  nanorod. Therefore, the structures of  $\text{CeO}_2$  with certain exposed facets have provided an ideal tool for the investigation of the synergistic

\* Corresponding author at: School of Environment, Tsinghua University, Beijing 100084, China.

\*\* Corresponding author.

E-mail addresses: [pengyue83@tsinghua.edu.cn](mailto:pengyue83@tsinghua.edu.cn) (Y. Peng), [lijunhua@tsinghua.edu.cn](mailto:lijunhua@tsinghua.edu.cn) (J. Li).

<https://doi.org/10.1016/j.apcatb.2018.06.024>

Received 2 March 2018; Received in revised form 6 June 2018; Accepted 8 June 2018

Available online 15 June 2018

0926-3373/© 2018 Published by Elsevier B.V.

effect among different components on supports.

Among the ceria-based bimetal oxides,  $\text{CoO}_x/\text{CeO}_2$  shows very good catalytic activity for the oxidation reactions, including the diesel soot oxidation, and catalytic combustion of VOCs. [5]. The excellent performance of  $\text{CoO}_x/\text{CeO}_2$  is attributed to the synergistic effect at the formed interfaces between  $\text{CoO}_x$  and  $\text{CeO}_2$ . Additionally, the most frequently used synthetic methods for  $\text{CoO}_x/\text{CeO}_2$  are the co-precipitation and impregnation methods [28–33]. The catalyst components are very complex with the use of these traditional research methods, and considerable controversy still exists for  $\text{CoO}_x/\text{CeO}_2$  with respect to the interface. Most researchers proposed that a strong interaction at the  $\text{CoO}_x/\text{CeO}_2$  interface led to higher oxygen diffusion from the bulk to the surface of  $\text{CeO}_2$ , which are key factors for catalytic performance [31]. While other researchers suggested a weak interaction at the  $\text{CoO}_x$  and  $\text{CeO}_2$  interface instead of a strong interaction was critical for catalytic oxidation, because the strong interaction at the interface inhibited the redox behavior of  $\text{CoO}_x$  via an oxygen supply from  $\text{CeO}_2$  at the interface. The results indicated that it was difficult to re-oxidize the cobalt species, which was disadvantageous for catalytic oxidation [5]. Hence, the different nanostructures of  $\text{CeO}_2$  provided an ideal tool to reveal the various synergistic effects at these interfaces.

Herein, low content of  $\text{CoO}_x$  supported on nanocrystal  $\text{CeO}_2$  with different morphologies were prepared and investigated for toluene oxidation. Ceria supports, including nanoparticles, nanorods, and nanocubes, were used and compared, with and without cobalt loading. The catalytic activities of  $\text{CoO}_x/\text{CeO}_2$  are dramatically influenced by the shape of  $\text{CeO}_2$ .  $\text{CoO}_x$  deposited on  $\text{CeO}_2$ -{111} nanoparticles is much more active than that on  $\text{CeO}_2$ -{110}/{100} nanorods and {100} nanocubes. Small highly dispersed nanoclusters of  $\text{CoO}_x$  formed on  $\text{CeO}_2$  nanoparticles, and a high concentration of oxygen vacancies formed at the  $\text{CoO}_x/\text{CeO}_2$  interface.

## 2. Experimental

### 2.1. Catalyst preparation

All the reagents were used without any further purification. The three different shapes of nanocrystalline  $\text{CeO}_2$  supports, namely, nanoparticles ( $\text{CeO}_2$ -P), nanorods ( $\text{CeO}_2$ -R) and nanocubes ( $\text{CeO}_2$ -C), were prepared by hydrothermal method. Then, a hydrothermal deposition technique was used to synthesis three  $\text{CoO}_x/\text{CeO}_2$  nanocatalysts, namely,  $\text{CoO}_x/\text{CeO}_2$  nanorods,  $\text{CoO}_x/\text{CeO}_2$  nanocubes, and  $\text{CoO}_x/\text{CeO}_2$  nanoparticles, denoted as  $\text{CoCe-R}$ ,  $\text{CoCe-C}$ , and  $\text{CoCe-P}$ , respectively. The cobalt loading was selected as 1 wt %, based on the  $[\text{Co}/\text{CeO}_2]_{\text{wt}} \times 100\%$ .

#### 2.1.1. Synthesis of three $\text{CeO}_2$ nanosupports

Three different shapes of  $\text{CeO}_2$  were prepared by the hydrothermal method. In brief, the  $\text{CeO}_2$ -P was obtained by hydrothermal synthesis. A certain amount of  $\text{Ce}(\text{NO}_3)_3 \cdot 6\text{H}_2\text{O}$  (5 mmol) (Aldrich, AR grade) and urea (50 mmol) (Sinopharm, AR grade) were dissolved with 80 mL deionized water in 100 mL Teflon bottle. The bottle was sealed tightly in a stainless steel autoclave and put into an oven at 180 °C, then kept for as long as 10 h without any disturbance. After that, turned off the oven, and left the autoclave naturally cooling down to room temperature. The sample was collected by centrifugal machine, then washed three times with deionized water, and dried at 90 °C for 12 h. The  $\text{CeO}_2$ -R was synthesized using an improved hydrothermal method [10]. In a typical procedure, 5 mmol  $\text{Ce}(\text{NO}_3)_3 \cdot 6\text{H}_2\text{O}$  (Aldrich, AR grade) was dissolved in 20 mL deionized water under stirring conditions. A NaOH solution (60 mL, 6 M) was added to the above solution and stirred for 30 min at room temperature. The solution in the Teflon bottle was then sealed tightly in a stainless steel autoclave. The hydrothermal condition was 120 °C for one day. Then the sample was collected by centrifugal machine, washed three times with deionized water, and dried at 90 °C for 12 h. Lastly, the  $\text{CeO}_2$ -C was synthesized the same as that for  $\text{CeO}_2$ -R

except that the hydrothermal treatment temperature was 180 °C. At last, all the dried precursors were calcined at 500 °C for 3 h in Muffle furnace with a heating rate of 2 °C/min.

#### 2.1.2. Synthesis of three $\text{CoO}_x/\text{CeO}_2$ nanocatalysts

Firstly,  $\text{Co}(\text{CH}_3\text{COO})_2$  (0.5 g) (Aldrich, AR grade) were dissolved in 80 mL of deionized water. The corresponding as prepared  $\text{CeO}_2$  nano-support was first ground for half an hour, then added into the above clear red solutions with ultrasound and stirring for 2 h. Subsequently, the obtained muddy slurry was transferred into a Teflon stainless steel autoclave and heated at 100 °C for 12 h. Finally, the sample was collected, washed three times with deionized water, and dried at 90 °C for 12 h. The three samples were calcined at 500 °C for 2 h in air.

#### 2.1.3. Synthesis of pure $\text{CoO}_x$ nanocatalyst

$\text{CoO}_x$  nanocatalyst was prepared by a published method [34]. 20 mL of  $\text{Co}(\text{NO}_3)_2 \cdot 6\text{H}_2\text{O}$  solution (0.37 M) was slowly added to 8 mL  $\text{Na}_2\text{CO}_3$  solution (1.25 M). The mixture was stirred for 12 h and then washed, filtered, and dried. Then the sample was calcined at 500 °C for 2 h in air.

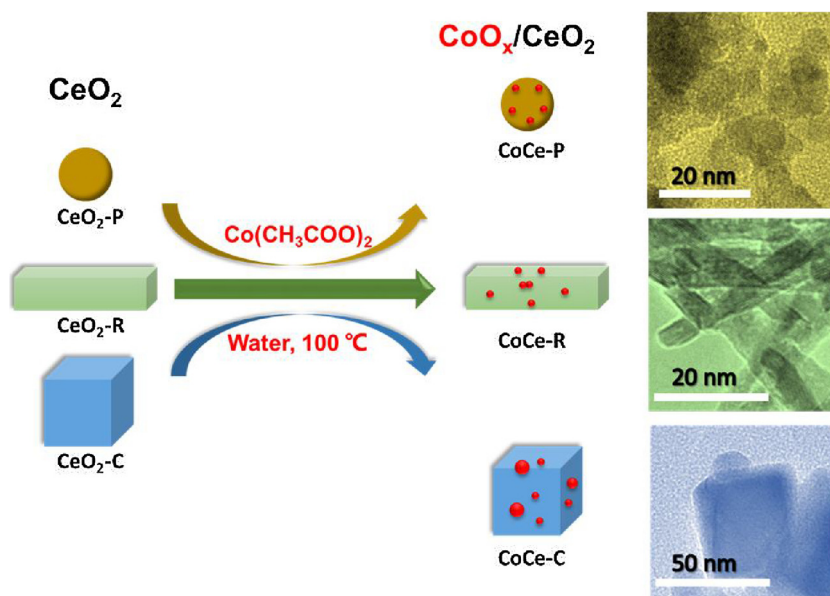
### 2.2. Catalyst characterization

The BET surface areas were estimated by  $\text{N}_2$  adsorption/desorption equilibrium curves at a liquid  $\text{N}_2$  temperature of  $-196$  °C using a Quantachrome Autosorb-1MP apparatus. The pore size distributions were measured by using desorption lines with the Barrett-Joyner-Halenda (BJH) method. XRD images were acquired via an X-ray diffractometer (Rigaku, D/max-2200) equipped with a Cu K $\alpha$  radiation source ( $\lambda = 0.15405$  nm, 200 mA and 40 kV). Raman spectroscopy was conducted using a Raman spectrometer (Renishaw RM2000, 532 nm). XPS analysis was performed with a multifunctional imaging electron spectrometer (ESCALAB 250XI, Thermo Scientific, U.K.) equipped with an Al K $\alpha$  radiation source ( $h\nu = 1486.6$  eV). Sample charging was corrected by setting the binding energy of adventitious carbon (C 1s) at 284.8 eV. All the TEM images were recorded on an electron microscope (JEM-2011, 200 kV). The analysis samples were prepared with full ultrasonic dispersion, and then the upper transparent liquid was placed onto a copper grid using a pipette. The energy-dispersive spectra (EDS) mapping images of all the samples were acquired by an EDS DX-4 analysis system.  $\text{H}_2$ -TPR profiles were acquired under a gas flow (10%  $\text{H}_2$  balanced with Ar, 50 mL/min) in a U-shaped quartz reactor with a Micromeritics Autochem 2720 instrument. Sample reduction was studied from 50 to 1000 °C in 10%  $\text{H}_2/\text{Ar}$  (50 mL/min) with a rate of 10 °C/min. The inductively coupled plasma atomic emission spectroscopy (ICP-AES) analyses of the samples were carried out using a Thermo IRIS spectrometer.

### 2.3. Catalyst evaluation

100 mg of the sample with 40–60 mesh was used to evaluate the catalytic oxidation of toluene in a continuous flow fixed-bed tube microreactor ( $\Phi = 10.0$  mm). The toluene vapor was generated and injected using a bubbler in a thermostatic bath at 0 °C, which passed through a container filled with liquid toluene. The reactant mixture (volumetric composition) consisted of 1000 ppm toluene and 20%  $\text{O}_2$  balanced in  $\text{N}_2$  with a total flow of 100 mL/min. At the beginning of each test, the catalyst was pretreated in the real reactant mixture for 1 h in order to overcome the over-estimation of toluene catalytic combustion conversion caused by adsorption of toluene. The performances at steady states (typically after 0.5 h for every 10 °C) were used for discussion. The concentrations of the reactants and the generation of the catalytic oxidation products were monitored in real time by a GC machine (Agilent 7890A) equipped with double flame ionization detectors (FID), where  $\text{CO}_2$  was detected by conversion into  $\text{CH}_4$  using a nickel methane reactor.

The toluene conversion (%) was calculated with the following



Scheme 1. Synthesis procedure for the synthesis of  $\text{CoO}_x/\text{CeO}_2$ .

formula:

$$\text{Toluene conversion (\%)} = \frac{[\text{Toluene}]_{\text{IN}} - [\text{Toluene}]_{\text{OUT}}}{[\text{Toluene}]_{\text{IN}}} \times 100\% \quad (1)$$

$[\text{Toluene}]_{\text{IN}}$  was the inlet toluene concentration,  $[\text{Toluene}]_{\text{OUT}}$  was the in outlet toluene concentration;

The normalized initial reaction rate ( $r$ ,  $\text{mol m}^{-2} \text{s}^{-1}$ ) was calculated as follows:

$$r = -\frac{F}{m \cdot S_{\text{BET}}} \cdot \frac{P}{RT} \cdot \ln(1-X) \cdot [\text{Toluene}]_{\text{IN}} \quad (2)$$

Where  $F$  was the toluene flow rate in unit of  $\text{mol s}^{-1}$ ,  $m$  was the catalyst amount,  $S_{\text{BET}}$  is the BET surface area.

### 3. Results and discussion

#### 3.1. Preparation procedure

Scheme 1 depicts a two-step preparation process including the hydrothermal synthesis of ceria nanorods, nanocubes, and nanoparticles and then the sequential introduction of  $\text{CoO}_x$  by a hydrothermal method. The three  $\text{CeO}_2$  nanostructures were obtained, and the corresponding TEM images are shown in Fig. S1. The XRD patterns of all the samples (Fig. S2) exhibited the specific diffraction peaks of standard  $\text{CeO}_2$  (JCPDS PDF # 43-1002); hence, the  $\text{CeO}_2$ -P,  $\text{CeO}_2$ -R and  $\text{CeO}_2$ -C samples exhibited a typical fluorite structure, and the average crystallite sizes of the three ceria nanosupports were calculated from the (111) plane by Scherrer's formula, and the results showed that the sequence of crystallite size was  $\text{CeO}_2$ -P (9 nm) <  $\text{CeO}_2$ -R (12 nm) <  $\text{CeO}_2$ -P (21 nm). In our work, three  $\text{CoO}_x/\text{CeO}_2$  samples were referred to as CoCe-P, CoCe-R and CoCe-C (the cobalt loading was selected as 1 wt%,  $[\text{Co}/\text{CeO}_2]_{\text{wt}} \times 100\%$ ). The ICP-AES results (Table 1) show that the experimental Co loadings of the CoCe-P, CoCe-R and CoCe-C catalysts are quite close to the target values.

#### 3.2. Characterization of $\text{CoO}_x/\text{CeO}_2$

Fig. 1 exhibits the XRD patterns of the three  $\text{CoO}_x/\text{CeO}_2$  catalysts. Compared with a standard  $\text{CeO}_2$  XRD pattern (JCPDS PDF # 43-1002), CoCe-P, CoCe-R and CoCe-C showed the typical fluorite structure of cerium dioxide. All of the three  $\text{CoO}_x/\text{CeO}_2$  samples had diffraction peaks at  $28^\circ$ ,  $33^\circ$ ,  $47^\circ$ ,  $56^\circ$ ,  $59^\circ$ ,  $69^\circ$ ,  $77^\circ$  and  $79^\circ$  ( $2\theta$ ), which correspond

Table 1

BET specific surface areas ( $S_{\text{BET}}$ ), crystallite sizes, and the  $A_{595}/A_{455}$  ratios from ICP-OES, Raman and XPS analyses ( $\text{Ce}^{3+}$  and  $\text{O}^\alpha$  mol %) of the catalysts.

Sample	Co (wt%) <sup>a</sup>	$S_{\text{BET}}$ ( $\text{m}^2 \text{g}^{-1}$ )	Crystallite size (nm) <sup>b</sup>	$\text{Ce}^{3+}$ (%) <sup>c</sup>	$\text{O}^\alpha$ (%) <sup>d</sup>	$r$ ( $10^{-8} \times \text{mol m}^{-2} \text{s}^{-1}$ ) <sup>e</sup>
CoCe-P	1.23	89	13	29	42	1.06
CoCe-R	1.02	85	15	22	38	0.10
CoCe-C	1.15	35	27	19	30	0.12

<sup>a</sup> Measured by ICP-AES.

<sup>b</sup> Calculated from the ceria (111) plane using Scherrer's formula.

<sup>c</sup>  $\text{Ce}^{3+}$  (%) =  $\text{Ce}^{3+}/(\text{Ce}^{3+} + \text{Ce}^{4+})$ , where  $\text{Ce}^{3+} = v_0 + v' + u_0 + u'$  and  $\text{Ce}^{4+} = v + v'' + v''' + u + u'' + u'''$ .

<sup>d</sup>  $\text{O}^\alpha$  (%) =  $\text{O}^\alpha/\text{O}^\beta$ .

<sup>e</sup> The reaction rate at  $220^\circ \text{C}$ .

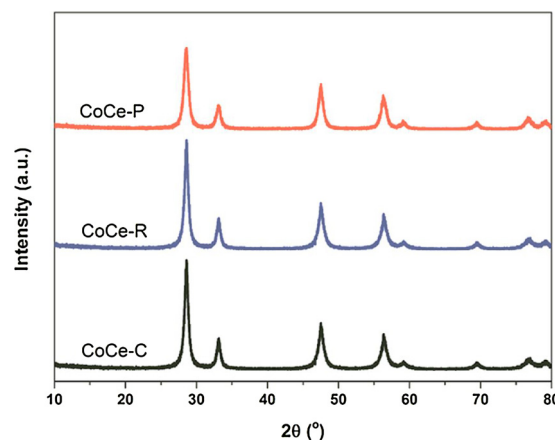


Fig. 1. Powder XRD patterns of the  $\text{CoO}_x/\text{CeO}_2$  nanocatalysts.

to the (111), (200), (220), (311), (222), (400), (331) and (420) planes of  $\text{CeO}_2$  respectively. Additionally, no XRD peaks were found for the cobalt oxides in the three catalysts [34,35], indicating the high dispersion of  $\text{CoO}_x$  or small  $\text{CoO}_x$  species on the  $\text{CeO}_2$  nanosupports. Furthermore, compared with CoCe-R and CoCe-C, the diffraction pattern of CoCe-P displayed weaker and broader features, which indicated that the crystal size of CoCe-P was smaller than that of CoCe-R or CoCe-

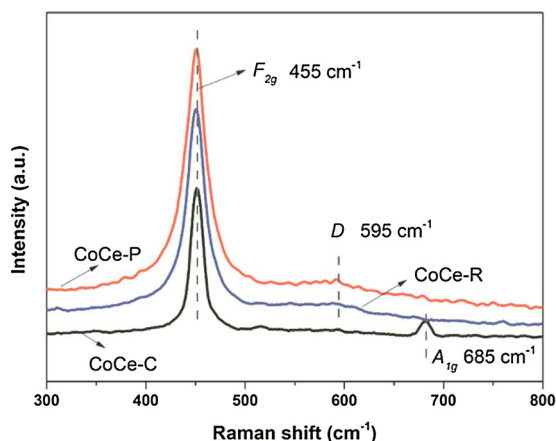


Fig. 2. The Raman patterns of the  $\text{CoO}_x/\text{CeO}_2$  nanocatalysts.

C. The average crystalline sizes of the three samples were calculated from the ceria (111) plane by Scherrer's formula, and the results (Table 1) showed that the sequence of crystallite size was still the same with the corresponding the pure ceria nanosupports.

As shown in Fig. 2, the state of cobalt on the surface of the as-prepared three  $\text{CoO}_x/\text{CeO}_2$  catalysts was investigated using Raman spectroscopy. The band at  $\sim 455 \text{ cm}^{-1}$  demonstrates the  $F_{2g}$  of a ceria fluorite-type structure, while the band at  $\sim 595 \text{ cm}^{-1}$  is assigned to the intrinsic oxygen vacancies due to the existence of  $\text{Ce}^{3+}$  in  $\text{CeO}_2$  [36,37]. It indicates that CoCe-P had the highest amount of oxygen defects, and CoCe-C had the smallest amount. Interestingly, a very small peak was found at  $\sim 685 \text{ cm}^{-1}$  for only the CoCe-C sample, which could be assigned to  $\text{CoO}_x$  [38]. While no bands assigned to the cobalt oxide species observed in CoCe-P and CoCe-R. This result revealed that the cobalt oxides were well dispersed in CoCe-P and CoCe-R, but not in CoCe-C.

The TEM images in Fig. 3 show that the nanoshaped  $\text{CoO}_x/\text{CeO}_2$  samples maintain their respective morphologies of the nanoshaped ceria supports. A typically image of the CoCe-P sample (Fig. 3a) revealed that the average nanoparticle size of CoCe-P was  $8 \pm 2 \text{ nm}$ . The HRTEM image of CoCe-P in Fig. 3b shows that only one type of interplanar spacing with  $0.32 \text{ nm}$  was observed, revealing that the surface of CoCe-P nanocatalysts were mainly dominated by {111} facets. Fig. 3d exhibited that CoCe-R consisted of nanorods with diameters of  $12 \pm 2 \text{ nm}$  and lengths of  $150\text{--}300 \text{ nm}$ . Fig. 3e exhibited a TEM image of CoCe-R with a high-resolution ratio, and two types of interplanar spacing of  $0.18$  and  $0.28 \text{ nm}$ , which meant that the lattice fringe directions for the (220) and (200) planes were consist for the surface structure of CoCe-R. The CoCe-R exhibited one-dimensional growth behavior, mainly exposed the unstable {110} and {100} type planes exposed as a surface terminating plane. These phenomena were very consistent with previous reports [10,35,39]. Fig. 3g showed the CoCe-C catalyst with a cubic structure ( $60\text{--}150 \text{ nm}$ ) together with some small random nanoparticles with sizes of ca.  $10 \text{ nm}$  on the surface of the ceria nanocube. Typical lattice fringe directions attributed to (200) planes were observed for CoCe-C in Fig. 3h, which had an interplanar spacing of  $0.28 \text{ nm}$ , means that the CoCe-C mainly exposed the unstable {100} type planes as a surface terminating plane. Additionally, the lattice fringe directions of (311) were observed with an interplanar spacing of  $0.25 \text{ nm}$  in these small random nanoparticles (Fig. 3h), revealing that the CoCe-C nanocomposite showed large cobalt oxide particles deposited on the nanocubes [40]. However, no such nanoparticles belong to the cobalt oxide particles found in the CoCe-P and CoCe-R samples, which revealed that the cobalt oxides were highly dispersed on the  $\text{CeO}_2$ -P and  $\text{CeO}_2$ -R nanoceria supports.

To further investigate the elemental distribution of Co in the three  $\text{CoO}_x/\text{CeO}_2$  nanostructures, elemental mapping analyses (as shown in

the right-most corner of Fig. 3) were conducted under the STEM-EDS mode. First, the CoCe-P and CoCe-R results are shown in Fig. 3c and f, which indicate that Co and Ce are uniformly distributed in the entire picture. This finding confirms that in the CoCe-P and CoCe-R samples, the ultralow content of cobalt oxides were highly dispersed on  $\text{CeO}_2$ -P and  $\text{CeO}_2$ -R. However, in CoCe-C (Fig. 3i), the EDX results showed that the Ce and Co atoms were not uniformly mixed, and there were very notable clusters of cobalt species, as indicated by a red oval. This finding indicates a lower cobalt oxide dispersion in CoCe-C compared with that of CoCe-P and CoCe-R. Again, it was proposed that the distribution of cobalt species on the surfaces of the nanocube {100} facets may not be as uniform as those on the nanorods (mainly {110} and {100} facets) and nanoparticles {111}. This result suggests that Co and Ce distribute well into CoCe-P and CoCe-R, and this type of uniform elemental distribution absolutely favors the interaction between  $\text{CeO}_2$  and  $\text{CoO}_x$ . This difference in cobalt distribution between the different  $\text{CeO}_2$  nanostructures reflects the different levels of interactions at the interface between the cobalt species and the  $\text{CeO}_2$  nanosupports. Hence, nanoceria with the most inert {111} plane compared with the well-known reactive {110} and {100}  $\text{CeO}_2$  planes could still be treated as a very active catalyst support with small particle sizes.

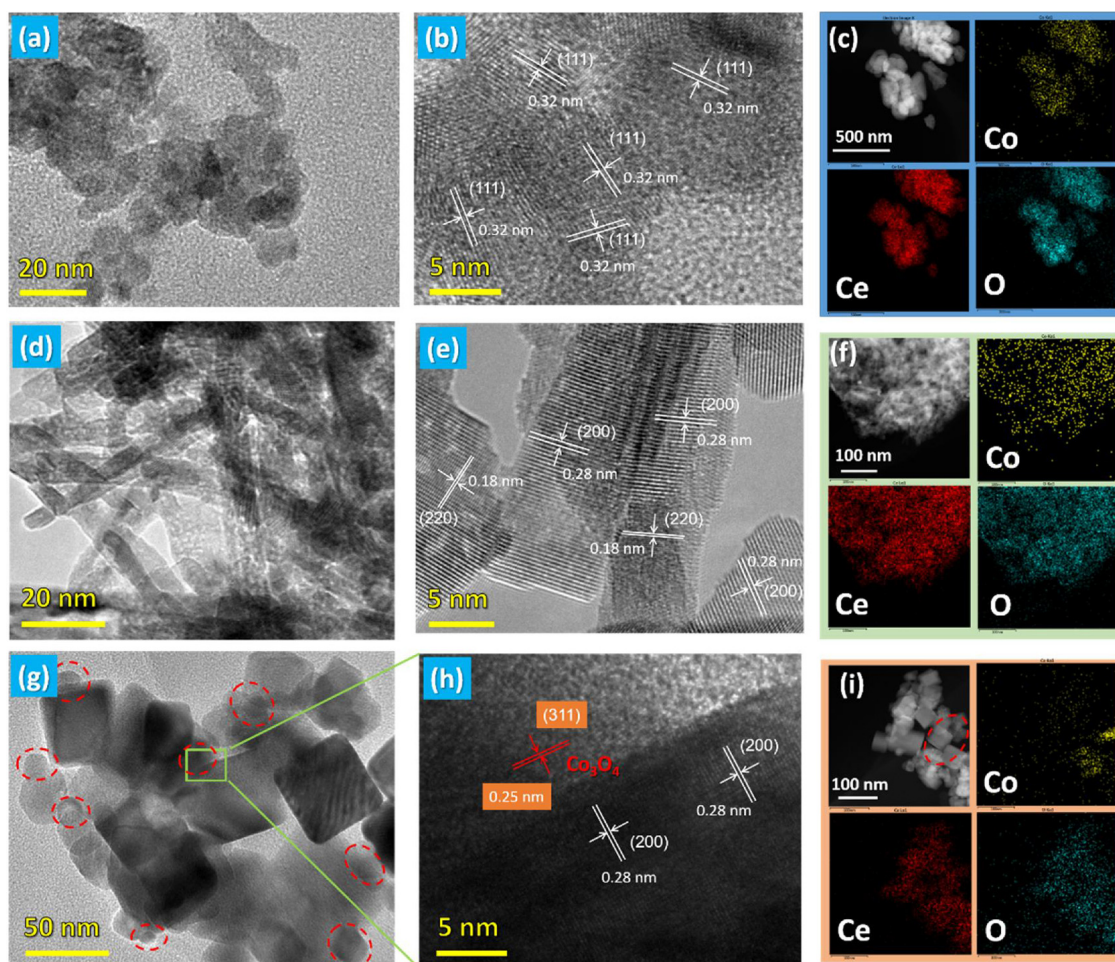
The related XPS spectra of Co 2p, Ce 3d, and O 1s of the three  $\text{CoO}_x/\text{CeO}_2$  catalysts are shown in Fig. 4. The two weak peaks that belong to Co 2p<sub>3/2</sub> ( $780.7 \text{ eV}$ ) and a satellite peak ( $786.7 \text{ eV}$ ) [40], respectively, were observed in Fig. 4a. However, the ultralow content of Co loading led to a very poor signal-to-noise feature of the pattern; hence, we could not accurately confirm the quantitative concentration of  $\text{Co}^{3+}$  and  $\text{Co}^{2+}$ . Moreover, the relative intensity of the Co 2p XPS spectra on CoCe-C was somewhat more prominent than that on CoCe-R and CoCe-P, further indicating a lower dispersion degree of cobalt in the sample. Considering the preparation procedure was the same for all the three samples, this behavior indicates that the effect of nano  $\text{CeO}_2$  in supports for the stabilization of  $\text{CoO}_x$  species must be quite different.

Fig. 4b exhibits typical Ce 3d spectra of the three samples, namely, CoCe-P, CoCe-R and CoCe-C. The Ce 3d patterns were fitted into ten main peaks according to previous reports, where the peaks marked as  $u/v$ ,  $u''/v''$  and  $u'''/v'''$  were attributed to the  $\text{Ce}^{4+}$  species, and the peaks denoted as  $u'/v'$ ,  $u_0/v_0$  were assigned to the  $\text{Ce}^{3+}$  species [41]. Interestingly, the Ce 3d<sub>5/2</sub> peaks of CoCe-P successively shifted to lower B.E. compared to that of CoCe-R, and CoCe-C showed the least, which indicates that the  $e$  cloud density around the Ce increased [42]. This increase means that more  $\text{Ce}^{3+}$  ions exist on the surface of the CoCe-P samples than on the CoCe-R and CoCe-C samples. In addition, according to the spectrum decomposition, the proportion of  $\text{Ce}^{3+}$  to the total Ce on the three  $\text{CoO}_x/\text{CeO}_2$  catalysts follows (Table 1) CoCe-P (29%) > CoCe-R (22%) > CoCe-C (19%). The higher the  $\text{Ce}^{3+}$  concentration is, the greater the formation of oxygen vacancies is [43]. This feature indicates that the amount of oxygen vacancies on CoCe-P were more than those on CoCe-R and CoCe-C.

Fig. 4c shows the O 1s XPS spectra. The O 1s spectra usually mainly consists of two types of O. The binding energy at  $531.0 \text{ eV}$  represents surface oxygen species ( $\text{O}^a$ ), and the binding energy at  $\sim 529.0 \text{ eV}$  refers to lattice oxygen species ( $\text{O}^b$ ). The concentration of  $\text{O}^a$  (based on the  $\text{O}^a/\text{O}^b$  ratio) in the three  $\text{CoO}_x/\text{CeO}_2$  samples follows (Table 1) CoCe-P (42%) > CoCe-R (38%) > CoCe-C (30%). This sequence indicates that the interaction of the cobalt species with the different exposed crystal planes of ceria results in the different behaviors of surface oxygen. This result implies that the surface oxygen content was greater on CoCe-P than on CoCe-R and CoCe-C.

To reveal the redox properties of the cobalt species interacting with different crystal planes of ceria,  $\text{H}_2$ -TPR was applied over the  $\text{CoO}_x/\text{CeO}_2$  catalysts. Fig. 5 exhibits the  $\text{H}_2$ -TPR profiles of the three  $\text{CoO}_x/\text{CeO}_2$  catalysts. Based on widely reported results, it is well known that  $\text{CeO}_2$  usually consists of two typical peaks: a low-temperature peak ca.  $500^\circ\text{C}$  (weak) and a high-temperature peak at  $800^\circ\text{C}$  (strong). The peak at  $500^\circ\text{C}$  is believed to result from surface oxygen reduction, while the





**Fig. 3.** TEM images of CoCe-P (a, b), CoCe-R (d, e), and CoCe-C (g, h). STEM images and EDX mappings of Co as well as the Ce and O distributions observed for the CoCe-P (c), CoCe-R (f), and CoCe-C (i) catalysts. The red circle highlights a large  $\text{CoO}_x$  cluster (For interpretation of the references to colour in this figure legend, the reader is referred to the web version of this article).

peak at 800 °C results from the reduction of bulk oxygen. The  $\text{H}_2$ -TPR result for  $\text{CoO}_x$  shows two peaks in the 300–450 °C region, as shown in Fig. S3. Normally, the low-temperature peak is attributed to the reduction of  $\text{CoO}_x$  to  $\text{CoO}$ , whereas the high-temperature peak can be assigned to the reduction of  $\text{CoO}$  to metallic Co [30,31,44]. Compared with the  $\text{H}_2$ -TPR profiles of the pure  $\text{CeO}_2$  and  $\text{CoO}_x$ , the main signals of three  $\text{CoO}_x/\text{CeO}_2$  nanostructures were greatly shifted toward lower temperatures in all the three samples, which implies that an ultralow content of  $\text{CoO}_x$  could lead to the greatly improvement of the low temperature reduction behavior [28,31]. For CoCe-P, the reduction peaks at approximately 300 °C were assigned to the reduction of  $\text{CoO}_x$ , and the reduction peak at 450 °C was attributed to the surface oxygen reduction of  $\text{CeO}_2$  [45]. Interesting, one reduction peak in the lower temperature region was observed for the CoCe-P catalyst, and this peak at 125 °C was due to the reduction of highly dispersed  $\text{CoO}_x$  species that weakly interact with  $\text{CeO}_2$  [30]. This finding suggests many synergistic interactions between  $\text{CoO}_x$  and  $\text{CeO}_2$  in CoCe-P, especially at the novel interface between these two components. For CoCe-R, only a single smooth feature is exhibited with a peak at 340 °C, which belongs to the reduction of well-dispersed  $\text{CoO}_x$  and the surface oxygen reduction of  $\text{CeO}_2$ . However, for CoCe-C, the multi-peak mountain-like signal means the reduction of different types of  $\text{CoO}_x$  species and also suggests that  $\text{CoO}_x$  mainly exists as large nanoparticles with different sizes when compared with CoCe-P and CoCe-R.

The existence of finely dispersed  $\text{CoO}_x$  species in close proximity to nanoceria can result in the best reducibility for the CoCe-P. The weakly interacting, highly dispersed of cobalt species on the {111} ceria

surface led to improved redox behavior for the cobalt species. Hence, there exists a synergistic effect at the interface between  $\text{CoO}_x$  and  $\text{CeO}_2$ .

### 3.3. Catalytic combustion performance of $\text{CoO}_x/\text{CeO}_2$

The toluene catalytic oxidation was studied over different  $\text{CoO}_x/\text{CeO}_2$  catalysts from 180 to 350 °C. During the entire temperature region, no toluene conversion was observed without the use of catalysts, whereas all the  $\text{CoO}_x/\text{CeO}_2$  nanocatalysts displayed toluene conversion into  $\text{CO}_2$ , as shown in Fig. 6. The toluene catalytic conversions over all three  $\text{CoO}_x/\text{CeO}_2$  catalysts exhibited typical S-shaped curves, and the toluene conversion increased with an increase in temperature. The toluene conversion over three corresponding pure  $\text{CeO}_2$  and pure  $\text{CoO}_x$  are shown in the Fig. 6. Normally, the low temperature activity of pure  $\text{CeO}_2$  was better than the corresponding  $\text{CoO}_x/\text{CeO}_2$  catalysts. However, the toluene conversion increased very slowly for all the pure  $\text{CeO}_2$  samples with increasing the temperature, and usually the corresponding  $\text{CoO}_x/\text{CeO}_2$  catalysts exhibited better catalytic behavior for the complete toluene conversion. In addition, the  $\text{CoO}_x$  nanocatalyst showed a very normal toluene catalytic oxidation performance (Fig. S4). It was obvious that CoCe-P exhibited the highest activity with a  $T_{50}$  (the reaction temperature of a toluene catalytic conversion of 50%) of approximately 212 °C, followed by CoCe-R (243 °C) and CoCe-C (272 °C). Additionally, compared with the least activity sample CoCe-C, the  $T_{50}$  for CoCe-P tremendously decreases by  $\Delta T_{50} = 60$  °C. The complete conversion temperature of toluene over the CoCe-R and CoCe-C catalysts was achieved at 300 and 350 °C, respectively. Meanwhile, the

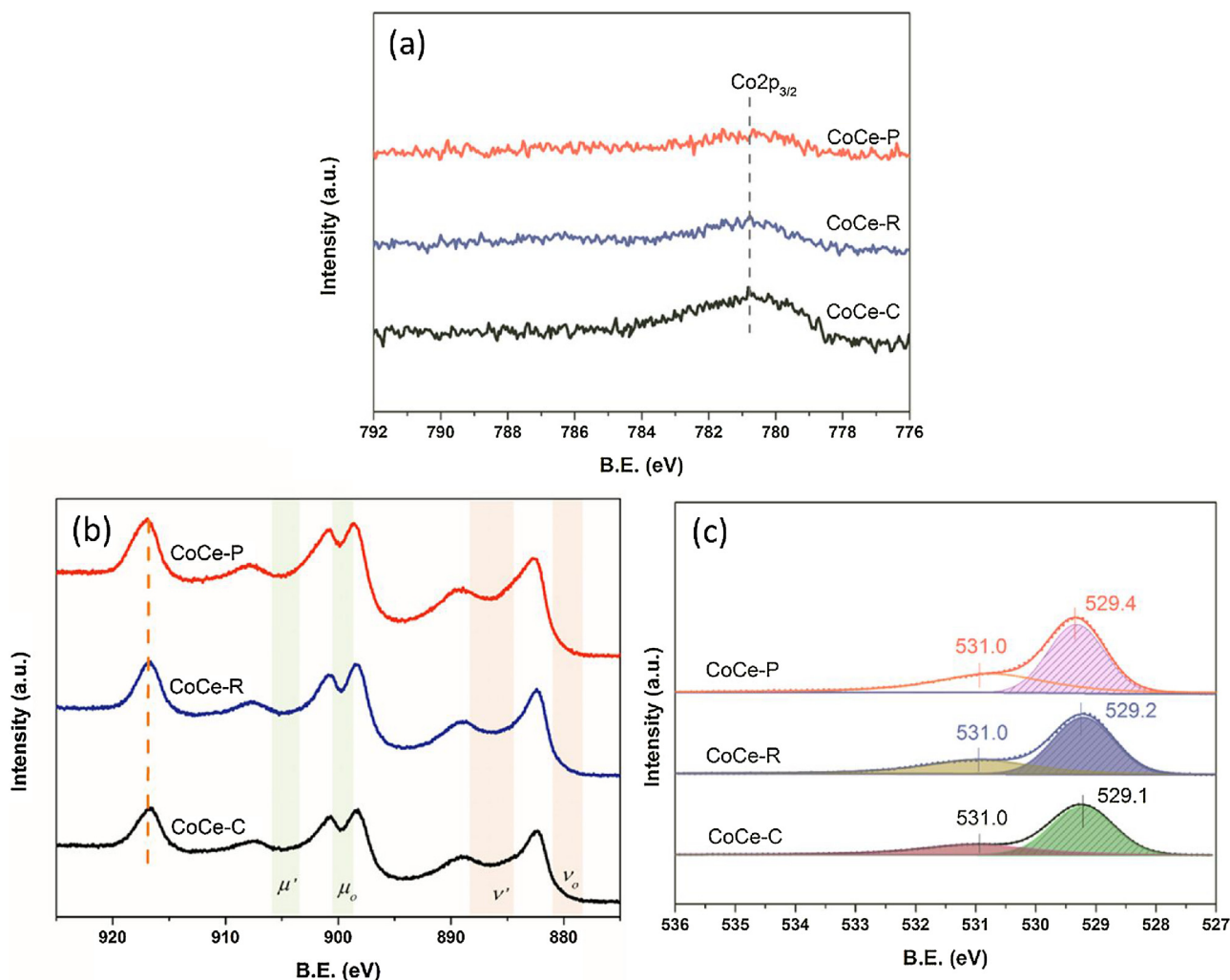


Fig. 4. Co 2p (a), Ce 3d (b), and O 1s (c) XPS spectra of the CoO<sub>x</sub>/CeO<sub>2</sub> nanostructures.

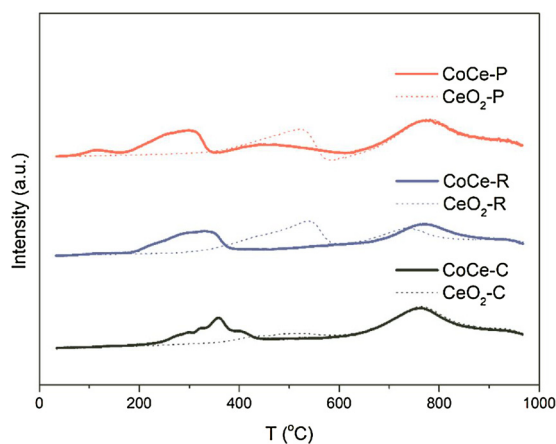


Fig. 5. H<sub>2</sub>-TPR profiles over the CoO<sub>x</sub>/CeO<sub>2</sub> nanostructures.

temperature over the CoCe-P was even lower than 240 °C.

For a more accurate evaluation of the factors that influence the toluene catalytic activity, the catalytic results are displayed as reaction rates normalized by the BET surface areas. We first assumed a first-order reaction for toluene and a zero-order for oxygen, and the calculated results are shown in Fig. 7. Below 210 °C, the performance behaviors of CoCe-P, CoCe-R and CoCe-C were very similar; however, at slightly higher temperatures, beginning with 220 °C, CoCe-P became

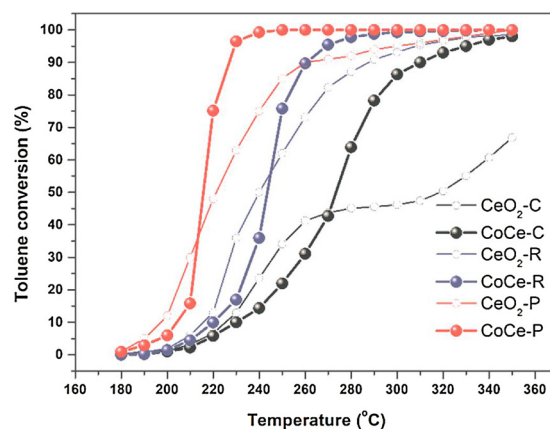


Fig. 6. Toluene conversion over different CoO<sub>x</sub>/CeO<sub>2</sub> and corresponding pure CeO<sub>2</sub>. Reaction conditions: 100 mL min<sup>-1</sup>, toluene 1000 ppm, 20 vol% O<sub>2</sub>, N<sub>2</sub> as balance gas, and GSHV = 60, 000 mL/(g h).

more active than CoCe-R and CoCe-C. The reaction rate ( $r$ , mol m<sup>-2</sup> s<sup>-1</sup>) of CoCe-P at 220 °C increased by a factor of 9 compared with that of CoCe-C. Hence, the catalytic activity indeed follows CoCe-P > CoCe-R > CoCe-C.

The surface oxygen vacancy formation and good oxygen mobility (the M-C mechanism) are mainly recognized as the key factors that influence the VOC catalytic oxidation activity [5,31,34]. In our study,

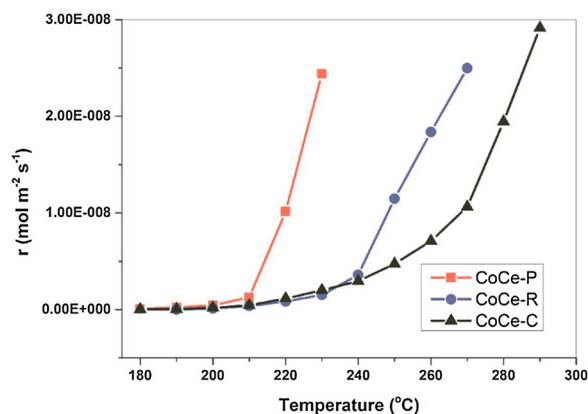


Fig. 7. The reaction rates over  $\text{CoO}_x/\text{CeO}_2$  nanocatalysts (normalized by the surface area of the catalysts).

we found that the good dispersion of the  $\text{CoO}_x$  spinel crystallites on the {111}  $\text{CeO}_2$  nanoparticles could be easily reduced. The highly dispersed  $\text{CoO}_x$  species at the {111} ceria surface led to more oxygen vacancies and an increase in the surface oxygen and oxygen mobility, which led to better redox behavior than that of the {100} and {110} surfaces. Although {111}  $\text{CeO}_2$  is the most inert plane compared with the well-known reactive {110} and {100}  $\text{CeO}_2$  planes, in the  $\text{CoO}_x/\text{CeO}_2$  nanocatalyst, the {111}  $\text{CeO}_2$  nanoparticles as the support can finely disperse the  $\text{CoO}_x$  species, which means more catalytically active sites. The presence of finely dispersed  $\text{CoO}_x$  species and the interaction between  $\text{CoO}_x$  and  $\text{CeO}_2$  are the main contributors to the high catalytic activity. Hence, the excellent performance of CoCe-P was due to the existence of suitably weak interactions at the  $\text{CoO}_x$  and  $\text{CeO}_2$  interface, leading to a high-concentration of oxygen vacancies at the interface and the improved redox behavior of the cobalt species, which is of great benefit to the low-temperature behavior of toluene catalytic oxidation.

### 3.4. Stability and water effect of CoCe-P

The catalytic stability of toluene oxidation is an important target for practical applications; therefore, we examined the most promising catalyst, namely, CoCe-P, in our current study. We examined the stability of CoCe-P during shutdown/restart operations and considered whether an environmental catalyst can endure temperature shock and withstand realistic conditions. In our test, the cyclic heating to 220 °C and then cooling to 180 °C was evaluated for 24 h on CoCe-P, as shown in Fig. 8. The following shutdown/restart procedure was used three times: After the operation was on-stream at 220 °C, it was then

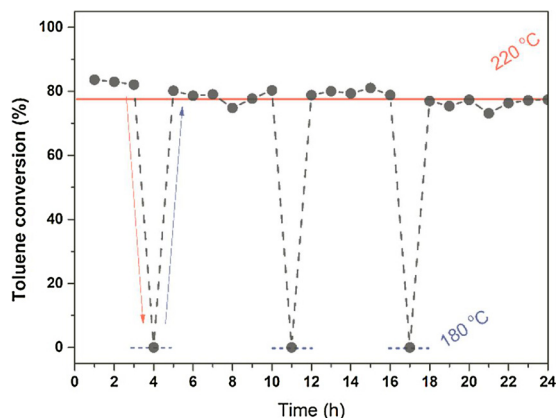


Fig. 8. Stability of CoCe-P in cyclic shutdown/restart tests: gas composition: toluene 1000 ppm, 20 vol%  $\text{O}_2$ ,  $\text{N}_2$  as the balance gas, and GHSV = 60, 000 mL/(g h).

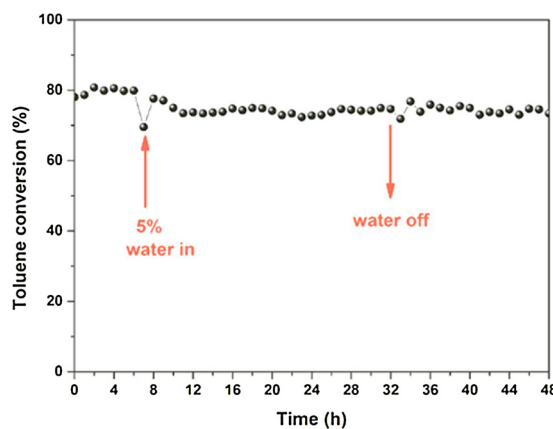


Fig. 9. Water effect of CoCe-P. Gas composition: toluene 1000 ppm, 20 vol%  $\text{O}_2$ , 5 vol.%  $\text{H}_2\text{O}$ ,  $\text{N}_2$  as the balance gas, 220 °C and GHSV = 60, 000 mL/(g h).

shutdown to 180 °C for 2 h, followed by reheating to 220 °C. The CoCe-P nanocatalyst did not suffer any obvious toluene catalytic activity loss during this harsh treatment. Hence, our CoCe-P nanocatalyst shows very good potential value for some practical applications, e.g., in fuel gas pollution control requiring frequent shutdowns during a typical operation.

Water always exists in VOC exhaust emission, and water vapor usually influences the performance of VOC catalytic oxidation [46]. Therefore, it is quite urgent to consider this effect in the research and development of a catalyst. Hence, the performance of toluene oxidation in the presence of water was evaluated over the most promising catalyst, CoCe-P. As shown in Fig. 9, a 48-h-long test under moist conditions at 220 °C with 5 vol%  $\text{H}_2\text{O}$  on CoCe-P has been investigated. We found that the water caused a decrease in the toluene conversion, but the conversion only decreased by 5% even after 48 h. One can see that after 5 vol.%  $\text{H}_2\text{O}$  was inserted into the stream, the conversion decreased quickly from 80% to 75% but then remained stable at 75%. However, once the  $\text{H}_2\text{O}$  was shut down, the toluene activity was still maintained at 75%. The performance of the sample with 5 vol%  $\text{H}_2\text{O}$  was almost identical to that of the removal condition, indicating that water had little effect on CoCe-P. Water has been widely treated as a typical poison in the catalytic oxidation of VOCs, for the loss of activity came from the competitive chemisorption of water on the active sites [47–49]; however, some recent studies also found that in some catalysts water contributes to improved catalytic behavior [28,31,50–54]. The initial result demonstrates that the CoCe-P catalyst shows very good hydrothermal stability.

## 4. Conclusions

In summary, three  $\text{CoO}_x/\text{CeO}_2$  with different ceria morphologies as supports (nanoparticle, nanorod, and nanocube) were prepared by a two-step hydrothermal method. Among the three  $\text{CoO}_x/\text{CeO}_2$  catalysts, the activity of toluene catalytic oxidation follows  $\text{CoCe-P} > \text{CoCe-R} > \text{CoCe-C}$ . The excellent performance of CoCe-P is due to the existence of suitably weak interaction at the  $\text{CoO}_x$  and  $\text{CeO}_2$  interface, leading to a high concentration of oxygen vacancies at the interface and the improved redox behavior of the cobalt species, which greatly benefit the low-temperature behavior of toluene catalytic oxidation. The {111}  $\text{CeO}_2$  catalyst is the most inert plane compared with the well-known reactive {110} and {100}  $\text{CeO}_2$  planes. However, in the  $\text{CoO}_x/\text{CeO}_2$  nano catalysts, the highly dispersed  $\text{CoO}_x$  species at the {111} nano  $\text{CeO}_2$  surface exhibits better redox behavior than that of the {100} and {110} surfaces. Hence, the exposed faces of ceria are irrelevant to determine the interface behavior and catalytic properties of the  $\text{CoO}_x/\text{CeO}_2$  catalysts. The highly active interfacial structures, even on an inert crystal plane, could be open up new possibilities in the design of highly



active ceria-based catalysts.

## Acknowledgments

This work was financially supported by the National Key Research and Development Program (2017YFC0211303), the National Natural Science Foundation of China (21777081).

## Appendix A. Supplementary data

Supplementary material related to this article can be found, in the online version, at doi:<https://doi.org/10.1016/j.apcatb.2018.06.024>.

## References

- [1] S. Wang, J. Hao, J. Environ. Sci. 24 (2012) 2–13.
- [2] K. Na, K.-C. Moon, Y.P. Kim, Atmos. Environ. 39 (2005) 5517–5524.
- [3] A.L. Bolden, C.F. Kwiatkowski, T. Colborn, Environ. Sci. Technol. 49 (2015) 5261–5276.
- [4] Z. Zhang, Z. Jiang, W. Shanguan, Catal. Today 264 (2016) 270–278.
- [5] L.F. Liotta, H. Wu, G. Pantaleo, A.M. Venezia, Catal. Sci. Technol. 3 (2013) 3085–3102.
- [6] H. Huang, Y. Xu, Q. Feng, D.Y. Leung, Catal. Sci. Technol. 5 (2015) 2649–2669.
- [7] Z. Qiao, Z. Wu, S. Dai, ChemSusChem 6 (2013) 1821–1833.
- [8] T. Montini, M. Melchionna, M. Monai, P. Fornasiero, Chem. Rev. 116 (2016) 5987–6041.
- [9] D. Zhang, X. Du, L. Shi, R. Gao, Dalton Trans. 41 (2012) 14455–14475.
- [10] H.X. Mai, L.D. Sun, Y.W. Zhang, R. Si, W. Feng, H. Zhang, H. Liu, C.H. Yan, J. Phys. Chem. B 109 (2005) 24380–24385.
- [11] L. Liu, Z. Yao, Y. Deng, F. Gao, B. Liu, L. Dong, ChemCatChem 3 (2011) 978–989.
- [12] H. Huang, Q. Dai, X. Wang, Appl. Catal. B-Environ. 158–159 (2014) 96–105.
- [13] E. Aneggi, D. Wiaters, C. de Leitenburg, J. Llorca, A. Trovarelli, ACS Catal. 4 (2014) 172–181.
- [14] T. Désaunay, G. Bonura, V. Chiodo, S. Freni, J.P. Couzinié, J. Bourgon, A. Ringuedé, F. Labet, C. Adamo, M. Cassir, J. Catal. 297 (2013) 193–201.
- [15] K. Wu, L.-D. Sun, C.H. Yan, Adv. Energy Mater. 6 (2016) 1600501.
- [16] A. Trovarelli, J. Llorca, ACS Catal. 7 (2017) 4716–4735.
- [17] R. Si, M. Flytzani-Stephanopoulos, Angew. Chem. Int. Ed. 120 (2008) 2926–2929.
- [18] D. Jiang, W. Wang, S. Sun, L. Zhang, Y. Zheng, ACS Catal. 5 (2015) 613–621.
- [19] Y. Gao, W. Wang, S. Chang, W. Huang, ChemCatChem 5 (2013) 3610–3620.
- [20] Z. Hu, X. Liu, D. Meng, Y. Guo, Y. Guo, G. Lu, ACS Catal. 6 (2016) 2265–2279.
- [21] R. Peng, X. Sun, S. Li, L. Chen, M. Fu, J. Wu, D. Ye, Chem. Eng. J. 306 (2016) 1234–1246.
- [22] P. Sudarsanam, B. Hillary, M.H. Amin, S.B.A. Hamid, S.K. Bhargava, Appl. Catal. B-Environ. 185 (2016) 213–224.
- [23] L. Torrente-Murciano, R.S. Chapman, A. Narvaez-Dinamarca, D. Mattia, M.D. Jones, PhysChemChemPhys 18 (2016) 15496–15500.
- [24] R.K. Singha, A. Shukla, A. Yadav, L.N. Sivakumar Konathala, R. Bal, Appl. Catal. B-Environ. 202 (2017) 473–488.
- [25] X. Du, D. Zhang, L. Shi, R. Gao, J. Zhang, J. Phys. Chem. C 116 (2012) 10009–10016.
- [26] G. Chen, Q. Xu, Y. Yang, C. Li, T. Huang, G. Sun, S. Zhang, D. Ma, X. Li, ACS Appl. Mater. Interfaces 7 (2015) 23538–23544.
- [27] M. Zabilskiy, P. Djinić, E. Tchernychova, O.P. Tkachenko, L.M. Kustov, A. Pintar, ACS Catal. 5 (2015) 5357–5365.
- [28] M. Kang, M. Song, C. Lee, Appl. Catal. A-Gen. 251 (2003) 143–156.
- [29] J. Luo, M. Meng, Y. Zha, L. Guo, J. Phys. Chem. C 112 (2008) 8694–8701.
- [30] J. Luo, M. Meng, X. Li, X. Li, Y. Zha, T. Hu, Y. Xie, J. Zhang, J. Catal. 254 (2008) 310–324.
- [31] L.F. Liotta, G. Di Carlo, G. Pantaleo, A.M. Venezia, G. Deganello, Appl. Catal. B-Environ. 66 (2006) 217–227.
- [32] C. Ma, D. Wang, W. Xue, B. Dou, H. Wang, Z. Hao, Environ. Sci. Technol. 45 (2011) 3628–3634.
- [33] S.M. Vickers, R. Gholami, K.J. Smith, M.J. MacLachlan, ACS Appl. Mater. Interfaces 7 (2015) 11460–11466.
- [34] B. Bai, H. Arandiyani, J. Li, Appl. Catal. B-Environ. 142–143 (2013) 677–683.
- [35] J. Mei, Y. Ke, Z. Yu, X. Hu, Z. Qu, N. Yan, Chem. Eng. J. 320 (2017) 124–134.
- [36] J. Li, Z. Zhang, W. Gao, S. Zhang, Y. Ma, Y. Qu, ACS Appl. Mater. Interfaces 8 (2016) 22988–22996.
- [37] Y. Lee, G. He, A.J. Akey, R. Si, M. Flytzani-Stephanopoulos, I.P. Herman, J. Am. Chem. Soc. 133 (2011) 12952–12955.
- [38] G. Chen, Q. Xu, Y. Wang, G. Song, C. Li, W. Zhao, W. Fan, Catal. Sci. Technol. 6 (2016) 7273–7279.
- [39] K. Zhou, X. Wang, X. Sun, Q. Peng, Y. Li, J. Catal. 229 (2005) 206–212.
- [40] M.M. Natile, A. Glisenti, Chem. Mater. 17 (2005) 3403–3414.
- [41] H. Borchert, Y.V. Frolova, V.V. Kaichev, I.P. Prosvirin, G.M. Alikina, A.I. Lukashevich, V.I. Zaikovskii, E.M. Moroz, S.N. Trukhan, V.P. Ivanov, J. Phys. Chem. C 109 (2005) 5728–5738.
- [42] D. Jiang, W. Wang, L. Zhang, Y. Zheng, Z. Wang, ACS Catal. 5 (2015) 4851–4858.
- [43] M.A. Henderson, C.L. Perkins, M.H. Engelhard, S. Thevuthasan, C.H.F. Peden, Surf. Sci. 526 (2003) 1–18.
- [44] J. Li, C. Ma, X. Xu, J. Yu, Z. Hao, S. Qiao, Environ. Sci. Technol. 42 (2008) 8947–8951.
- [45] G. Grzybek, P. Stelmachowski, S. Gudyka, P. Indyka, Z. Sojka, N. Guillén-Hurtado, V. Rico-Pérez, A. Bueno-López, A. Kotarba, Appl. Catal. B-Environ. 180 (2016) 622–629.
- [46] S. Zhao, F. Hu, J. Li, ACS Catal. 6 (2016) 3433–3441.
- [47] H. Nassiri, K.E. Lee, Y. Hu, R.E. Hayes, R.W. Scott, N. Semagina, J. Catal. 352 (2017) 649–656.
- [48] F. Hu, J. Chen, Y. Peng, H. Song, K. Li, J. Li, Chem. Eng. J. 331 (2018) 425–434.
- [49] S. Xie, H. Dai, J. Deng, Y. Liu, H. Yang, Y. Jiang, W. Tan, A. Ao, G. Guo, Nanoscale 5 (2013) 11207–11219.
- [50] D.R. Mullins, Surf. Sci. Rep. 70 (2015) 42–85.
- [51] S.M. Saqer, D.I. Kondarides, X.E. Verykios, Appl. Catal. B-Environ. 103 (2011) 275–286.
- [52] L. Nie, D. Mei, H. Xiong, B. Peng, Z. Ren, X.I.P. Hernandez, D. Andrew, M. Wang, H.M. Engelhard, L. Kovarik, A.K. Datye, Y. Wang, Science 358 (2017) 1419–1423.
- [53] Y. Wang, L. Guo, M. Chen, C. Shi, Catal. Sci. Technol. (2018), <https://doi.org/10.1039/C7CY01867C>.
- [54] C. Wang, X.K. Gu, H. Yan, Y. Lin, J. Li, D. Liu, W.X. Li, J. Lu, ACS Catal. 7 (2016) 887–891.